Journal of Nuclear Medicine, published on April 30, 2021 as doi:10.2967/jnumed.120.261594

First-in-human PET imaging and estimated radiation dosimetry of L-[5-^{11}C]-glutamine in patients with metastatic colorectal cancer

Authors: Allison S. Cohen[1,2,†,*] , Joe Grudzinski[3], Gary T. Smith[4,5], Todd E. Peterson[2,4], Jennifer G. Whisenant[6,7], Tiffany L. Hickman[7], Kristen K. Ciombor[6,7], Dana Cardin[6,7], Cathy Eng[6,7], Laura W. Goff[6,7], Satya Das[6,7], Robert J. Coffey[6,7,8], Jordan D. Berlin[6,7], and H. Charles Manning[1,2,4,7,†,**]

[1]Vanderbilt Center for Molecular Probes, Vanderbilt University Medical Center, Nashville, TN

[2]Vanderbilt University Institute of Imaging Science, Vanderbilt University Medical Center, Nashville, TN

[3]Internal Dosimetry Consultants, LLC, Madison, WI

[4]Department of Radiology and Radiological Sciences, Vanderbilt University Medical Center, Nashville, TN

[5]Nuclear Medicine, Tennessee Valley Healthcare System, Nashville VA Medical Center, Nashville, TN

[6]Department of Medicine, Vanderbilt University Medical Center, Nashville, TN

[7]Vanderbilt-Ingram Cancer Center, Vanderbilt University Medical Center, Nashville, TN

[8]Department of Cell and Developmental Biology, Vanderbilt University, Nashville, TN

[†]Current address: Department of Cancer Systems Imaging, The University of Texas MD Anderson Cancer Center, Houston, TX

*First author: Allison S. Cohen, Ph.D.

Address: Department of Cancer Systems Imaging, The University of Texas MD Anderson Cancer Center, 1515 Holcombe Blvd., 3SCR4.3430, Unit 1907, Houston, TX 77030

Phone: (713) 794-4324

Fax: (713) 794-5456

E-mail: ascohen1@mdanderson.org

**Corresponding author: H. Charles Manning, Ph.D.

Address: Department of Cancer Systems Imaging, Center for Advanced Biomedical Imaging (CABI), The University of Texas MD Anderson Cancer Center, 1515 Holcombe Blvd. 3SCR4.3626, Unit 1907, Houston, TX 77030

Phone: (713) 563-4872

Fax: (713) 794-5456

E-mail: hcmanning@mdanderson.org

Short running title: First-in-human PET using ^{11}C-Glutamine

Word Count: 6,223 words

Financial Statement: This work was supported by grants from the NIH (P30 CA068485, P50 CA236733, U24 CA220325, R35 CA197570, S10 OD019963, and S10 OD012297) and generous philanthropic funding from the Julia Reed Foundation, Debbie and Michael Rose Discovery Grant, and Samuel K. and Sandra G. Wellborn Cancer Discovery Grant. HCM is a Cancer Prevention Research Institute of Texas (CPRIT) Scholar in Cancer Research and is supported by CPRIT RR200046.

Abstract

Altered metabolism is a hallmark of cancer. In addition to glucose, glutamine is an important nutrient for cellular growth and proliferation. Non-invasive imaging via positron emission tomography (PET) may help facilitate precision treatment of cancer through patient selection and monitoring of treatment response. L-[5-^{11}C]-glutamine (^{11}C-glutamine) is a PET tracer designed to study glutamine uptake and metabolism. The aim of this first-in-human study was to evaluate the radiologic safety and biodistribution of ^{11}C-glutamine for oncologic PET imaging.

Methods: Nine patients with confirmed metastatic colorectal cancer underwent PET/computed tomography (CT) imaging. Patients received 337.97 $\pm$ 44.08 MBq of ^{11}C-glutamine. Dynamic PET acquisitions centered over the abdomen or thorax were initiated simultaneously with intravenous tracer administration. Following the dynamic acquisition, a whole-body PET/CT was acquired. Volume-of-interest analyses were carried out to obtain estimates of organ-based absorbed doses of radiation.

Results: ^{11}C-glutamine was well-tolerated in all patients with no observed safety concerns. Organs with the highest radiation exposure included the bladder, pancreas, and liver. The estimated effective dose was 4.46E-03 $\pm$ 7.67E-04 mSv/MBq. Accumulation of ^{11}C-glutamine was elevated and visualized in lung, brain, bone, and liver metastases, suggesting utility for cancer imaging.

Conclusion: PET using ^{11}C-glutamine appears safe for human use and allows non-invasive visualization of metastatic colon cancer lesions in multiple organs. Further studies are needed to elucidate its potential for other cancers and for monitoring response to treatment.

Keywords: ^{11}C-glutamine, metabolism, PET, colorectal cancer

Introduction

Altered metabolism has been shown to be important for cancer cell growth and proliferation (*1,2*). Conventional metabolic imaging has focused primarily on the role of glucose through positron emission tomography (PET) imaging with ^{18}F-fluorodeoxyglucose (^{18}F-FDG). However, studies have demonstrated the importance of additional metabolic pathways (*2-8*). This feature of cancer has led to the development of metabolism-targeted imaging and therapeutic strategies focused on pathways other than glycolysis (*3-5,7-14*). Non-invasive molecular imaging with novel PET tracers is increasingly being deployed in clinical oncology. Targeting tumor-specific pathways represents a promising approach for improved PET imaging of tumors.

Glutamine represents an important metabolic substrate that is dysregulated in cancer (*3-9,11-14*). Glutamine metabolism allows for energy production via adenosine triphosphate, anaplerosis through the tricarboxylic acid cycle, defense against oxidative stress via glutathione, and biosynthesis of other amino acids and nucleotides (*3-9,12*). In oncology, glutamine is primarily transported into cells by ASCT2, the sodium-dependent neutral amino acid transporter encoded by *SLC1A5*. ASCT2 is overexpressed in a number of cancer types (*12-14*), which has been linked to poor survival (*13*). Imaging of glutamine could be complementary to ^{18}F-FDG imaging by identifying tumors that either are ^{18}F-FDG-negative or in locations with high background ^{18}F-FDG uptake (*7*). In addition, glutamine imaging could provide further information about the cancer's underlying biology. Finally, it could serve as a tool for new therapies targeting glutamine metabolism (*15,16*).

Synthesis of both ^{18}F- and ^{11}C-labeled glutamine have been reported (*17-27*). ^{18}F-glutamine has been studied preclinically (*28-39*) and clinically (*31,36,40-43*). However, the distribution and metabolism of ^{18}F-glutamine differs from the naturally occurring substrate and it is prone to defluorination *in vivo* (*28,31,40*). L-[5-^{11}C]-glutamine (^{11}C-glutamine) is chemically and biologically identical to physiological glutamine. Cells that avidly take up glutamine will also avidly take up ^{11}C-glutamine, thereby providing a direct marker of glutamine transport and the first step of glutaminolysis. ^{11}C-glutamine has been studied in preclinical mouse models (*21*) but to date has not been studied in humans. Here, we report the first-in-human studies using ^{11}C-glutamine in a clinical trial of patients with colorectal cancer.

Materials and Methods

Patients

Patients were prospectively enrolled in a clinical trial conducted at Vanderbilt University Medical Center (VUMC, ClinicalTrials.gov identifier: NCT03263429) and underwent baseline (pre-treatment) PET/computed tomography (CT) imaging. The trial was approved by VUMC's Institutional Review Board and all subjects provided informed consent before participating in the study. The study was conducted in accordance with the Helsinki Declaration and the Health Insurance Portability and Accountability Act. All patients were ≥18 years old, had a histologically or cytologically-confirmed diagnosis of metastatic wildtype *KRAS* colorectal cancer, and had received prior anti-epidermal growth factor receptor therapy. In addition,

patients had undergone baseline evaluation of disease status by CT or magnetic resonance imaging and had at least one measurable lesion as defined by RECIST 1.1.

^{11}C-Glutamine Production

^{11}C-glutamine (L-[5-^{11}C]-glutamine) was synthesized by the VUMC Radiochemistry Core facility as previously described (*27*). ^{11}C-glutamine was synthesized under cGMP conditions with approval from the VUMC Radioactive Drug Research Committee. ^{11}C-glutamine met all USP <823> requirements for a sterile, injectable PET radiopharmaceutical. Quality control included analysis of radiochemical and chemical purities, residual solvent content, endotoxin content, pH, filter integrity, radionuclidic purity, and appearance. Sterility testing was performed post-release. The production method utilized (*27*) yields mass levels below 800 μg, which falls several orders of magnitude below reported safe dose levels (*44-46*). Molar activity was not measured given that these mass levels fall below the detection limit of the instrumentation.

Imaging Protocol

Images were acquired using a Philips Vereos PET/CT scanner with patients lying in the supine position. A dynamic imaging protocol was conducted prior to a whole-body protocol. Patients were asked to fast for at least 6 hours prior to tracer injection and blood glucose levels were tested prior to administration of radioactivity. PET scan data acquisition was initiated simultaneously with intravenous injection of ^{11}C-glutamine injected over 30 seconds. The mean administered activity was 337.97 $\pm$ 44.08 MBq (range, 232.36-386.98 MBq). Dynamic emission images were acquired over the tumor region of interest using six 1-minute scans, six 2-minute

scans, six 5-minute scans, and one 10-minute scan for a total scan duration of 58 minutes scanning time, as tolerated by the patient. A whole body (vertex of skull to mid-thighs) PET scan was then conducted using 9 bed positions, at 2 minutes per bed position, for a total scan time of ~18 minutes. Prior to and accompanying each PET image exam, a brief, low-energy, whole body transmission CT scan without contrast (120 KVp, 25 mAs, and 4.0-mm slice thickness) was collected for attenuation correction and anatomic localization. PET images were reconstructed using iterative ordered subset expectation maximization (15 subsets, 3 iterations) with all corrections applied. The reconstructed PET image had a 4-mm slice thickness and a 169×169 transaxial matrix with a 4-mm pixel spacing. Patients were monitored during and 24 hours following the PET scan for any reactions or adverse events. Side effects and reactions were graded per Common Terminology Criteria for Adverse Events 4.03 criteria. There were no adverse or clinically detectable pharmacologic effects in any of the 9 subjects.

Image Analysis

Maximum intensity projection (MIP) images and fusion of PET images with accompanying CT were performed using OsiriX (Pixmeo, Bernex, Switzerland). Regions of interest were drawn over lesions, normal liver, and left ventricle blood pool. The ratios of the maximum value in the lesion to the average value in the blood pool from whole-body images were documented for each lesion of patients shown in the figures. The ratios of the maximum value in the lesion to the average value in the normal liver from whole-body images are given for liver lesions shown in the figures. A volume of interest (VOI) analysis was performed for both the dynamic and whole-body imaging protocols using the Inveon Research Workplace 4.2 (Siemens Medical

Solutions USA). For analysis of the dynamic PET images, VOIs were drawn over the organs which were within the dynamic PET protocol's field of view (FOV), which consisted of one bed position and spanned either the lungs or the abdomen. The mean activity concentration (Bq/mL) in each VOI was decay corrected to the beginning of the study to generate time-activity curves (TACs) over the duration of the scan. Those patients whose abdomen was within the PET FOV during the dynamic PET protocol were suitable for radiation dosimetry estimation. For the whole-body imaging protocol, VOIs were drawn over organs throughout the entire body. The mean concentration (Bq/mL) and standard uptake value (SUV) using the patient's body weight (SUV_{bw}) were calculated for each VOI.

Patient to Phantom Data Conversion

To convert patient %ID/g ($[\%ID/g]_{Patient}$) values to phantom whole-organ %ID/organ ($[\%ID/organ]_{Phantom}$) for use in estimating whole-organ cumulative activities, Eq. 1 was used:

$$[\%ID/organ]_{Phantom} = [\%ID/g]_{Patient} \cdot TBM_{Patient} \cdot \frac{OM_{Phantom}}{TBM_{Phantom}} \quad \text{Eq. 1}$$

where $TBM_{Patient}$ is the total body mass of the patient, $OM_{Phantom}$ is the phantom organ mass (from OLINDA organ mass listing (*47,48*) and Reference Man (ICRP 23) (*49*)), and $TBM_{Phantom}$ is the phantom total body mass (adult male = 74 kg; adult female = 57 kg). This approach assumes that the concentration of activity in a tissue relative to the overall concentration in the whole-body is preserved when translating from patient to phantom.

Cumulative Activity Calculation

Cumulative activity for each organ was calculated from the biokinetic curves of the dynamic PET scans by first multiplying each point by $e^{-\lambda_{phys}t}$, where λ_{phys} = decay constant for C-11, 2.04 hr^{-1} , and t, the post-injection time of the data point. Piecewise numerical integration using the trapezoidal method was used to calculate the cumulative activity for each organ. The cumulative activity from $t = 0$, t_0, to the final time point, t_f, $\tilde{A}_{t_0 \to t_f}$, [Bq-h], was calculated by numerically integrating the tissue radioactivity using the trapezoidal rule in Eq. 2:

$$\tilde{A}_{t_0 \to t_f} = \int_{t_0}^{t_f} A(t) \approx \sum_{i=t_0}^{t_f - 1} (t_{i+1} - t_i)\left(\frac{A(t_{i+1}) + A(t_i)}{2}\right). \quad \text{Eq. 2}$$

The cumulative activity from the time of the final scan time point, t_f, to time infinity, t_∞, $\tilde{A}_{t_f \to t_\infty}$, [Bq-h] was calculated by integrating the exponential decay after the last time point to infinity the physical decay constant, λ_{phys},:

$$\tilde{A}_{t_f \to t_\infty} = \int_{t_f}^{t_\infty} A(t) = \int_{t_f}^{t_\infty} \exp\left(-\lambda_{phys} t\right) = \mathrm{A(t_f)}/\lambda_{phys}, \quad \text{Eq. 3}$$

The total cumulative activity, $\tilde{A}_{t_0 \to t_\infty}$, [Bq-h] was then calculated by summing $\tilde{A}_{t_0 \to t_f}$ and $\tilde{A}_{t_f \to t_\infty}$:

$$\tilde{A}_{t_0 \to t_\infty} = \tilde{A}_{t_0 \to t_f} + \tilde{A}_{t_f \to t_\infty}. \quad \text{Eq. 4}$$

The number of decays per injected activity [Bq-h/Bq] was computed for each organ by dividing the cumulative activity by the injected activity [Bq]. Furthermore, the number of decays per injected activity for the 'remainder' was computed by subtracting the sum of organ cumulative activities from the total number of decays from 1 Bq of [C-11] assuming only physical decay.

$$\tilde{A}_{t_0 \to t_\infty remainder} = 1\ \mathrm{Bq}/\lambda_{phys} - \sum_{organs} \tilde{A}_{t_0 \to t_\infty}. \qquad \text{Eq. 5}$$

Absorbed Dose Estimation

Given the residence times, OLINDA v1.1 (*48*) was used to estimate the absorbed doses in adult phantoms. Absorbed dose per injected activity (mGy/MBq) was estimated for all organs of interest. The decays in the bladder were assumed to equal the decay-corrected whole-body fraction of injected activity in the bladder for the whole-body PET scan multiplied by τ, where τ= 1 Bq/λ_{phys}, 0.49 hr.

Results

Safety and Biodistribution

Baseline ^{11}C-glutamine imaging data from nine patients were evaluated. There were no signs of toxicity or observed adverse events following injection of ^{11}C-glutamine. Whole-body PET analysis in normal organs included evaluation of uptake in salivary glands, heart, bladder,

liver, spleen, kidneys, pancreas, stomach, small intestine, lungs, muscle, fat, brain, bone marrow, testis, and adrenals (Figure 1 and Supplemental Figure 1). The highest signal was observed for the bladder as expected due to excretion of the tracer. High activity was also seen in the pancreas and liver. Examination of the time-activity curves (TACs) show distinctive clearance profiles for different organs (Supplemental Figure 2). High initial activity was seen in the kidneys (Supplemental Figures 2A and 2B), spleen (Supplemental Figure 2C), and heart (Supplemental Figure 2D) with rapid clearance observed in all of these organs. The liver showed a gradual increase in activity up to 5-15 minutes followed by a slow washout (Supplemental Figure 2E), whereas uptake in the pancreas increased up to 11-13 minutes and then plateaued (Supplemental Figure 2F). There was low intestinal uptake with activity peaking rapidly and then remaining stable up to the end of the dynamic scan (Supplemental Figure 2G). Large variability was seen in the ^{11}C-glutamine TACs in the bone marrow of these patients (Supplemental Figure 2H). There was variable uptake in the adrenals for different patients, but all of the curves followed the same pattern (Supplemental Figure 2I).

Estimated Absorbed Dose

The average number of decays per injected activity (Bq-h/Bq) for each organ are provided in Table 1. Table 2 provides average absorbed dose per injected activity (mGy/MBq) for adult subjects. The mean ± standard deviation (SD) effective dose for ^{11}C-glutamine was 4.46E-03 ± 7.67E-04 mSv/MBq. The organs with highest doses were the liver (1.68E-02 ± 4.69E-03 mGy/MBq), pancreas (1.30E-02 ± 2.64E-03 mGy/MBq), and bladder wall (1.14E-02 ± 3.45E-

03 mGy/MBq). The only organ whose coefficient of variation was greater than 30% was the adrenal glands with 35%.

Uptake in Metastatic Lesions

Accumulation of ^{11}C-glutamine exceeded background in several lesions across subjects presenting with pulmonary metastases (Figures 2A, 2B, 3C, and 3D and Supplemental Figure 3D) and hepatic metastases (Figure 4C). Visualization of normal organ accumulation for a representative patient illustrating high uptake in the bladder, liver, and pancreas is shown in the whole-body images (Figures 3A and B). ^{11}C-glutamine uptake in hepatic lesions was oftentimes at the periphery with a photopenic center, which existed on a high background of normal accumulation (Figures 4A, B, and C). Some liver metastases and an adrenal mass were indistinguishable from background liver accumulation but could be imaged with an alternative tracer of glutamine metabolism (Supplemental Figures 3A, 3B, 3C, and Supplemental Figure 4) (*50,51*). Skeletal metastases were also observed (Figures 4A, B, and D). Interestingly, previously unidentified brain metastases were seen in two patients (Figure 2C) which were subsequently confirmed using standard imaging (Figure 2D). Glutamine-avid lesions typically exhibited rapid accumulation following injection, which either plateaued or gradually decreased over time (Figure 4E). Representative ^{11}C-glutamine tumor uptake values (lesion-to-blood pool ratios) are given in Table 3.

Discussion

The role of altered metabolism in cancer progression is increasingly recognized (*1,2*). Altered glucose metabolism is a well-known phenomenon, but recently there has been growing emphasis on other pathways including amino acid metabolism. As the most abundant amino acid in the plasma, glutamine has been shown to be vital to the growth and survival of certain cancers (*3-9,11-14*). Thus, glutaminolysis has emerged as a novel therapeutic target (*3,4,7-9,11-14*). However, methods to predict responders or monitor response to these new therapies are lacking. Novel imaging methods can be developed as biomarkers to meet this unmet need and aid in the pursuit of precision approaches to oncology. Previous studies have reported imaging with ^{11}C-labeled glutamine in preclinical models (*21*). Here, we present the clinical translation of this agent.

As part of this first-in-human study, we evaluated the safety and biodistribution of ^{11}C-glutamine in patients with metastatic colorectal cancer. ^{11}C-glutamine was found to be safe with no adverse side effects observed at the dose employed in this study. Uptake of ^{11}C-glutamine was highest in the bladder, liver, and pancreas. High uptake in the pancreas is consistent with previously reported biodistribution studies in mice (*21*). This uptake was attributed to the exocrine function and high protein turnover within the pancreas. Additionally, clearance profiles were comparable to those published in mice with the heart and kidneys demonstrating rapid uptake and clearance, whereas the liver showed a slower washout rate (*21*). Excretion through the bladder was also observed preclinically. The biodistribution pattern of ^{11}C-glutamine is consistent with the human biodistribution of another ^{11}C-labeled amino acid, L-[methyl-^{11}C]methionine (*52*).

Use of ^{11}C-glutamine has a number of potential advantages, including the opportunity to leverage the short half-life of carbon-11 to follow other orthogonal metabolic pathways through simple sequential imaging protocols (*51*). While certain technical advantages are inherent to the fluorinated agent, ^{18}F-(*2S, 4R*)-4-fluoroglutamine, this tracer and ^{11}C-glutamine differ with respect to metabolic fate. For example, accumulated ^{18}F-(*2S, 4R*)-4-fluoroglutamine remains as the parent compound, with a small fraction resulting from metabolites (*28,31,34,40,43*). Only a percentage is incorporated into biomolecules (*28,29,34,38,40*). An aliphatic fluoride-labeled analogue, ^{18}F-(*2S, 4R*)-4-fluoroglutamine is also prone to defluorination *in vivo* (*28,31,37,38,40,43*). In contrast, ^{11}C-glutamine is metabolized to ^{11}C-glutamate and ^{11}C-CO_2 (*53*), as well as incorporated directly into biomolecules (*21*). Generally, imaging with ^{11}C-glutamine reports on both uptake and downstream metabolism, while uptake of ^{18}F-(*2S, 4R*)-4-fluoroglutamine is likely more representative of glutamine transport (*34*). Thus, while ^{11}C-glutamine behaves identically to the naturally occurring substrate, this also represents a potential limitation of this tracer for PET imaging as the signal detected will be from all radioactively labelled molecules including the parent ligand and a range of metabolic intermediates.

The mean ± SD effective dose for ^{11}C-glutamine was 4.46E-03 ± 7.67E-04 mSv/MBq. While a full range of timepoints across the whole body were not collected in this study, our calculated value is comparable to other reported effective doses for ^{11}C-labeled PET tracers (*52,54-57*). This effective dose is similar to those reported for other ^{11}C-labeled amino acid radiopharmaceuticals (*52,54,55*) and a magnitude lower than dose estimates for ^{18}F-labeled radiopharmaceuticals found in the literature (*50,58-62*) due mainly to the short half-life of

carbon-11. This value compares well with the mean effective dose (5.9E-03 ± 2.0E-03 mSv/MBq) reported in a review of 37 dose estimates for ^{11}C-labeled PET tracers (*56*) and with the average effective dose (5.2E-03 ± 1.7E-03 mSv/MBq) from a recent review of 77 literature publications for a wide range of ^{11}C-labeled tracers (*57*). It is approximately one fourth the average effective dose (2.05E-02 ± 7.6E-03 mSv/MBq) found from a review of 144 publications for a range of ^{18}F-labeled tracers (*57*). The effective dose estimate for ^{11}C-glutamine is about four-fold less compared to ^{18}F-(*2S, 4R*)-4-fluoroglutamine (*42*). Because the magnitude of the SUVs of the two radiotracers are very similar (*40*), the difference in dosimetry can be mainly attributed to the difference in physical half-lives.

^{11}C-glutamine enabled the visualization of tumor lesions in various metastatic sites, including the liver, lungs, bones, and brain. Consistent with this data, prior human studies with ^{18}F-(*2S, 4R*)-4-fluoroglutamine also showed tracer uptake in brain, bone, and lung metastases (*40,41,43*). Uptake of ^{18}F-(*2S, 4R*)-4-fluoroglutamine in the normal liver was more intense than liver lesions, with the tumor sites appearing as cold spots (*41*). This matches the uptake pattern we observed for many of the liver lesions in our study using ^{11}C-glutamine. In hepatic metastases, normal liver uptake can exceed tumor uptake making it difficult to define tumor lesions. This represents a potential limitation of these tracers. A potential advantage of ^{11}C-glutamine could be in the detection of bone metastases, as these lesions could be missed with ^{18}F-(*2S, 4R*)-4-fluoroglutamine due to normal uptake in the bone marrow of free ^{18}F resulting from defluorination of the tracer (*41*). ^{18}F-(*2S, 4R*)-4-fluoroglutamine enabled visualization of breast cancer lymph node metastases as well (*36,42*). Utility of ^{11}C-glutamine in other cancer types was not evaluated in this work and will be the focus of future studies. Not all lesions

identified in these patients were glutamine avid. Thus, ^{11}C-glutamine PET may inform each metastatic tumor's underlying metabolism and biology. This intra-patient tumoral heterogeneity emphasizes the need for a non-invasive means of diagnosing and staging patients. In addition, it points to the importance of using multiple orthogonal approaches to studying cancer. Imaging with ^{11}C-glutamine can complement other imaging approaches, including ^{18}F-FDG PET and PET imaging with other tracers currently in development, thus providing a more complete picture of the patient's disease and underlying biological processes in individual metastatic sites. The use of total body PET scanners could also potentially result in images with higher sensitivity for lesion detection and improved kinetic parameter estimation by enabling simultaneous dynamic imaging of multiple organs or lesions (*63-65*). However, these scanners are still under development and not yet widely available.

One limitation of this study is the small sample size and evaluation within a focused clinical context (metastatic colorectal cancer). In addition, full quantitative analyses of tumor uptake were not performed. Thus, the diagnostic utility of ^{11}C-glutamine PET in colorectal cancer remains to be determined and is a future area of investigation. It is likely that other solid tumors may be effectively imaged with this tracer, which may also provide insight into tumors that may be sensitive to certain metabolically-targeted therapies such as inhibitors of glutaminase activity (*16*) or glutamine transport (*15*). The utility of ^{11}C-glutamine PET to image tumors beyond colorectal cancer and for monitoring of treatment response should be the focus of future works.

Conclusion

This clinical study demonstrates that ^{11}C-glutamine is well-tolerated in human subjects. PET imaging with ^{11}C-glutamine is feasible and elevated uptake was seen in lesions of patients with metastatic colorectal cancer. The estimated dosimetry is consistent with other ^{11}C-labeled tracers. Thus, further use of this tracer is warranted. Larger clinical studies will provide additional information and could demonstrate the utility of ^{11}C-glutamine for imaging in a variety of cancer types and for measurement of treatment response.

Disclosure: The authors have no relevant disclosures. This work was supported by grants from the NIH (P30 CA068485, P50 CA236733, U24 CA220325, R35 CA197570, S10 OD019963, and S10 OD012297) and generous philanthropic funding from the Julia Reed Foundation, Debbie and Michael Rose Discovery Grant, and Samuel K. and Sandra G. Wellborn Cancer Discovery Grant. No potential conflicts of interest relevant to this article exist.

Acknowledgments

The authors thank the patients and their families for participation in this study. Anna Fisher and Adam Rosenberg are acknowledged for experimental and manuscript support. The VUMC/VUIIS Human Imaging and Radiochemistry Core facilities assisted with PET and preparation of the radiotracer.

Key Points

Question:

Is ^{11}C-glutamine safe and suitable for PET imaging of human cancer?

Pertinent findings:

This study evaluated the safety and biodistribution of ^{11}C-glutamine and analyzed its ability to visualize metastatic lesions in patients with colorectal cancer. ^{11}C-glutamine was well-tolerated and showed increased uptake in tumors relative to background.

Implications for Patient Care:

Imaging with ^{11}C-glutamine may advance precision medicine by enabling the characterization of tumors non-invasively by PET and may serve as a predictive and prognostic biomarker in future studies.

References

1. Hanahan D, Weinberg RA. Hallmarks of cancer: the next generation. *Cell.* 2011;144:646-674.

2. Pavlova NN, Thompson CB. The emerging hallmarks of cancer metabolism. *Cell Metab.* 2016;23:27-47.

3. Kishton RJ, Rathmell JC. Novel therapeutic targets of tumor metabolism. *Cancer J.* 2015;21:62-69.

4. Sai KKS, Zachar Z, Bingham PM, Mintz A. Metabolic PET imaging in oncology. *AJR Am J Roentgenol.* 2017;209:270-276.

5. Pantel AR, Ackerman D, Lee SC, Mankoff DA, Gade TP. Imaging cancer metabolism: underlying biology and emerging strategies. *J Nucl Med.* 2018;59:1340-1349.

6. DeBerardinis RJ, Cheng T. Q's next: the diverse functions of glutamine in metabolism, cell biology and cancer. *Oncogene.* 2010;29:313-324.

7. Rajagopalan KN, DeBerardinis RJ. Role of glutamine in cancer: therapeutic and imaging implications. *J Nucl Med.* 2011;52:1005-1008.

8. Choi YK, Park KG. Targeting glutamine metabolism for cancer treatment. *Biomol Ther (Seoul).* 2018;26:19-28.

9. Altman BJ, Stine ZE, Dang CV. From Krebs to clinic: glutamine metabolism to cancer therapy. *Nat Rev Cancer.* 2016;16:619-634.

10. Sun A, Liu X, Tang G. Carbon-11 and fluorine-18 labeled amino acid tracers for positron emission tomography imaging of tumors. *Front Chem.* 2017;5:124.

11. Zhu L, Ploessl K, Zhou R, Mankoff D, Kung HF. Metabolic imaging of glutamine in cancer. *J Nucl Med.* 2017;58:533-537.

12. Scalise M, Pochini L, Galluccio M, Console L, Indiveri C. Glutamine transport and mitochondrial metabolism in cancer cell growth. *Front Oncol.* 2017;7:306.

13. Liu Y, Zhao T, Li Z, Wang L, Yuan S, Sun L. The role of ASCT2 in cancer: a review. *Eur J Pharmacol.* 2018;837:81-87.

14. Jiang H, Zhang N, Tang T, Feng F, Sun H, Qu W. Target the human Alanine/Serine/Cysteine Transporter 2 (ASCT2): achievement and future for novel cancer therapy. *Pharmacol Res.* 2020;158:104844.

15. Schulte ML, Fu A, Zhao P, et al. Pharmacological blockade of ASCT2-dependent glutamine transport leads to antitumor efficacy in preclinical models. *Nat Med.* 2018;24:194-202.

16. Cohen AS, Geng L, Zhao P, et al. Combined blockade of EGFR and glutamine metabolism in preclinical models of colorectal cancer. *Transl Oncol.* 2020;13:100828.

17. Qu W, Zha Z, Ploessl K, et al. Synthesis of optically pure 4-fluoro-glutamines as potential metabolic imaging agents for tumors. *J Am Chem Soc.* 2011;133:1122-1133.

18. Zhang X, Basuli F, Shi ZD, et al. Automated synthesis of [(18)F](2S,4R)-4-fluoroglutamine on a GE TRACERlab FX-N Pro module. *Appl Radiat Isot.* 2016;112:110-114.

19. Li S, Schmitz A, Lee H, Mach RH. Automation of the radiosynthesis of six different (18)F-labeled radiotracers on the AllinOne. *EJNMMI Radiopharm Chem.* 2017;1:15.

20. Zhang Y, Zhang L, Yang J, et al. Initial experience in synthesis of (2S,4R)-4-[(18) F]fluoroglutamine for clinical application. *J Labelled Comp Radiopharm.* 2019;62:209-214.

21. Qu W, Oya S, Lieberman BP, et al. Preparation and characterization of L-[5-11C]-glutamine for metabolic imaging of tumors. *J Nucl Med.* 2012;53:98-105.

22. Gleede T, Riehl B, Shea C, et al. Investigation of S(N)2 [C-11]cyanation for base-sensitive substrates: an improved radiosynthesis of L-[5-C-11]-glutamine. *Amino Acids.* 2015;47:525-533.

23. Nasr K, Xin YC, Rydberg N, Hallgren R, Cai HC, Sun XK. Improved automated production for clinical use of C-11-L-glutamine [abstract]. *J Nucl Med.* 2017;58 (suppl 1):872.

24. Padakanti P, Schmitz A, Lee S, Mankoff D, Mach R. Synthesis of carbon-11 labelled L-glutamine on Synthra HCN synthesis module [abstract]. *J Nucl Med.* 2017;58 (suppl 1):1025.

25. Padakanti PK, Li S, Schmitz A, Mankoff D, Mach RH, Lee HS. Automated synthesis of [(11)C]L-glutamine on Synthra HCN plus synthesis module. *EJNMMI Radiopharm Chem.* 2019;4:5.

26. Rosenberg A, Nickels M, Schulte M, Manning HC. Automated clinical product of [11C] glutamine on commercial synthesis modules [abstract]. *J Nucl Med.* 2017;58 (suppl 1):332.

27. Rosenberg AJ, Nickels ML, Schulte ML, Manning HC. Automated radiosynthesis of 5-[C-11]L-glutamine, an important tracer for glutamine utilization. *Nucl Med Biol.* 2018;67:10-14.

28. Lieberman BP, Ploessl K, Wang L, et al. PET imaging of glutaminolysis in tumors by 18F-(2S,4R)4-fluoroglutamine. *J Nucl Med.* 2011;52:1947-1955.

29. Ploessl K, Wang L, Lieberman BP, Qu W, Kung HF. Comparative evaluation of 18F-labeled glutamic acid and glutamine as tumor metabolic imaging agents. *J Nucl Med.* 2012;53:1616-1624.

30. Wu Z, Zha Z, Li G, et al. [(18)F](2S,4S)-4-(3-Fluoropropyl)glutamine as a tumor imaging agent. *Mol Pharm.* 2014;11:3852-3866.

31. Venneti S, Dunphy MP, Zhang H, et al. Glutamine-based PET imaging facilitates enhanced metabolic evaluation of gliomas in vivo. *Sci Transl Med.* 2015;7:274ra217.

32. Hassanein M, Hight MR, Buck JR, et al. Preclinical evaluation of 4-[18F]fluoroglutamine PET to assess ASCT2 expression in lung cancer. *Mol Imaging Biol.* 2016;18:18-23.

33. Schulte ML, Hight MR, Ayers GD, et al. Non-invasive glutamine PET reflects pharmacological inhibition of BRAF(V600E) in vivo. *Mol Imaging Biol.* 2017;19:421-428.

34. Zhou R, Pantel AR, Li S, et al. [(18)F](2S,4R)4-fluoroglutamine PET detects glutamine pool size changes in triple-negative breast cancer in response to glutaminase inhibition. *Cancer Res.* 2017;77:1476-1484.

35. Abu Aboud O, Habib SL, Trott J, et al. Glutamine addiction in kidney cancer suppresses oxidative stress and can be exploited for real-time imaging. *Cancer Res.* 2017;77:6746-6758.

36. Liu F, Xu X, Zhu H, et al. PET imaging of (18)F-(2S,4R)4-fluoroglutamine accumulation in breast cancer: from xenografts to patients. *Mol Pharm.* 2018;15:3448-3455.

37. Li C, Huang S, Guo J, et al. Metabolic evaluation of MYCN-amplified neuroblastoma by 4-[(18)F]FGln PET imaging. *Mol Imaging Biol.* 2019;21:1117-1126.

38. Miner MW, Liljenback H, Virta J, et al. (2S, 4R)-4-[(18)F]fluoroglutamine for in vivo PET imaging of glioma xenografts in mice: an evaluation of multiple pharmacokinetic models. *Mol Imaging Biol.* 2020;22:969-978.

39. Viswanath V, Zhou R, Lee H, et al. Kinetic modeling of (18)F-(2S,4R)4-fluoroglutamine in mouse models of breast cancer to estimate glutamine pool size as an indicator of tumor glutamine metabolism. *J Nucl Med.* December 4, 2020 [Epub ahead of print].

40. Dunphy MPS, Harding JJ, Venneti S, et al. In vivo PET assay of tumor glutamine flux and metabolism: in-human trial of (18)F-(2S,4R)-4-fluoroglutamine. *Radiology.* 2018;287:667-675.

41. Xu X, Zhu H, Liu F, et al. Imaging brain metastasis patients with 18F-(2S,4R)-4-fluoroglutamine. *Clin Nucl Med.* 2018;43:e392-e399.

42. Xu X, Zhu H, Liu F, et al. Dynamic PET/CT imaging of (18)F-(2S, 4R)4-fluoroglutamine in healthy volunteers and oncological patients. *Eur J Nucl Med Mol Imaging.* 2020;47:2280-2292.

43. Grkovski M, Goel R, Krebs S, et al. Pharmacokinetic assessment of (18)F-(2S,4R)-4-fluoroglutamine in patients with cancer. *J Nucl Med.* 2020;61:357-366.

44. Shao A, Hathcock JN. Risk assessment for the amino acids taurine, L-glutamine and L-arginine. *Regul Toxicol Pharmacol.* 2008;50:376-399.

45. Ward E, Picton S, Reid U, et al. Oral glutamine in paediatric oncology patients: a dose finding study. *Eur J Clin Nutr.* 2003;57:31-36.

46. Ziegler TR, Benfell K, Smith RJ, et al. Safety and metabolic effects of L-glutamine administration in humans. *JPEN J Parenter Enteral Nutr.* 1990;14:137S-146S.

47. Stabin MG, Siegel JA. Physical models and dose factors for use in internal dose assessment. *Health Phys.* 2003;85:294-310.

48. Stabin MG, Sparks RB, Crowe E. OLINDA/EXM: the second-generation personal computer software for internal dose assessment in nuclear medicine. *J Nucl Med.* 2005;46:1023-1027.

49. ICRP. *Report of the task group on reference man. ICRP Publication 23*. Oxford: Pergamon Press; 1975.

50. Smolarz K, Krause BJ, Graner FP, et al. (S)-4-(3-18F-fluoropropyl)-L-glutamic acid: an 18F-labeled tumor-specific probe for PET/CT imaging--dosimetry. *J Nucl Med.* 2013;54:861-866.

51. Kavanaugh G, Williams J, Morris AS, et al. Utility of [(18)F]FSPG PET to image hepatocellular carcinoma: first clinical evaluation in a US population. *Mol Imaging Biol.* 2016;18:924-934.

52. Deloar HM, Fujiwara T, Nakamura T, et al. Estimation of internal absorbed dose of L-[methyl-11C]methionine using whole-body positron emission tomography. *Eur J Nucl Med.* 1998;25:629-633.

53. Padakanti P, Pantel AR, Choi H, et al. Refined analysis of [11C]L-glutamine metabolism in triple negative breast cancer xenograft model. Paper presented at: World Molecular Imaigng Conference, 2020.

54. Tolvanen T, Nagren K, Yu M, et al. Human radiation dosimetry of [11C]MeAIB, a new tracer for imaging of system A amino acid transport. *Eur J Nucl Med Mol Imaging.* 2006;33:1178-1184.

55. Yao B, Tang C, Tang G, et al. Human biodistribution and radiation dosimetry of S-11C-methyl-L-cysteine using whole-body PET. *Clin Nucl Med.* 2015;40:e470-474.

56. van der Aart J, Hallett WA, Rabiner EA, Passchier J, Comley RA. Radiation dose estimates for carbon-11-labelled PET tracers. *Nucl Med Biol.* 2012;39:305-314.

57. Zanotti-Fregonara P, Lammertsma AA, Innis RB. (11)C dosimetry scans should be abandoned. *J Nucl Med.* 2021;62:158-159.

58. Deloar HM, Fujiwara T, Shidahara M, et al. Estimation of absorbed dose for 2-[F-18]fluoro-2-deoxy-D-glucose using whole-body positron emission tomography and magnetic resonance imaging. *Eur J Nucl Med.* 1998;25:565-574.

59. Graham MM, Peterson LM, Link JM, et al. Fluorine-18-fluoromisonidazole radiation dosimetry in imaging studies. *J Nucl Med.* 1997;38:1631-1636.

60. Vesselle H, Grierson J, Peterson LM, Muzi M, Mankoff DA, Krohn KA. 18F-fluorothymidine radiation dosimetry in human PET imaging studies. *J Nucl Med.* 2003;44:1482-1488.

61. Pauleit D, Floeth F, Herzog H, et al. Whole-body distribution and dosimetry of O-(2-[18F]fluoroethyl)-L-tyrosine. *Eur J Nucl Med Mol Imaging.* 2003;30:519-524.

62. Nye JA, Schuster DM, Yu W, Camp VM, Goodman MM, Votaw JR. Biodistribution and radiation dosimetry of the synthetic nonmetabolized amino acid analogue anti-18F-FACBC in humans. *J Nucl Med.* 2007;48:1017-1020.

63. Cherry SR, Badawi RD, Karp JS, Moses WW, Price P, Jones T. Total-body imaging: transforming the role of positron emission tomography. *Sci Transl Med.* 2017;9:eaaf6169.

64. Badawi RD, Shi H, Hu P, et al. First human imaging studies with the EXPLORER total-body PET scanner. *J Nucl Med.* 2019;60:299-303.

65. Pantel AR, Viswanath V, Daube-Witherspoon ME, et al. PennPET Explorer: human imaging on a whole-body imager. *J Nucl Med.* 2020;61:144-151.

Figures and Figure Legends

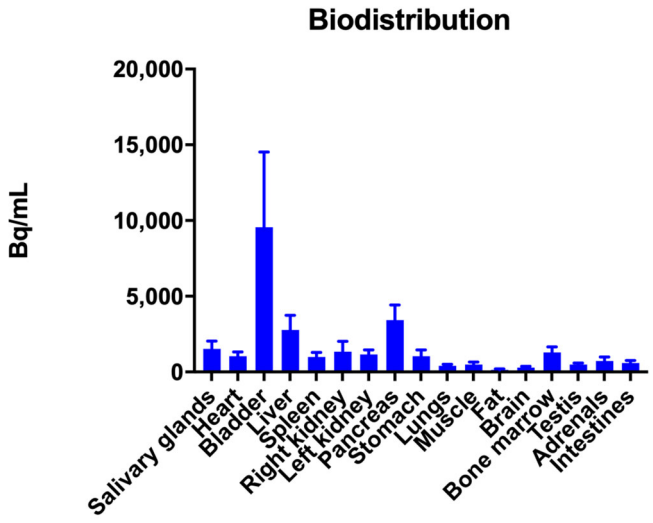

Figure 1: Whole-body biodistribution of ^{11}C-glutamine uptake in normal tissues. The activity concentration (Bq/mL) is plotted for 1-hour post-injection.

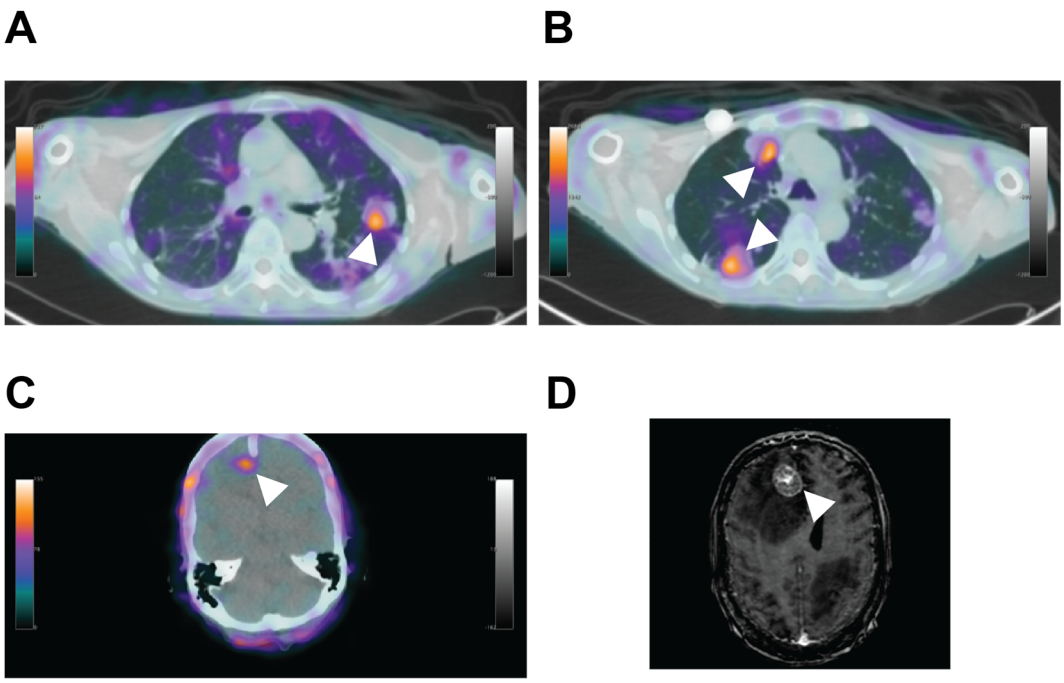

Figure 2: ^{11}C-glutamine tumor uptake in a patient with metastatic colorectal cancer. Axial ^{11}C-glutamine PET/CT fusion images corresponding to a left lung metastasis (**A**), two right lung metastases (**B**), and a brain metastasis (**C**). White arrowheads point to the lesions. The lesion-to-blood pool ratios from the whole-body scan were 2.64 (**A**), 2.22 (**B**, top arrow), 2.35 (**B**, bottom arrow) and 1.68 (**C**). (**D**) A contrast-enhanced MRI was obtained 6.5 weeks post-baseline PET imaging and treatment. The lesion is indicated with a white arrowhead. The MRI confirms the presence of the brain lesion seen with ^{11}C-glutamine PET.

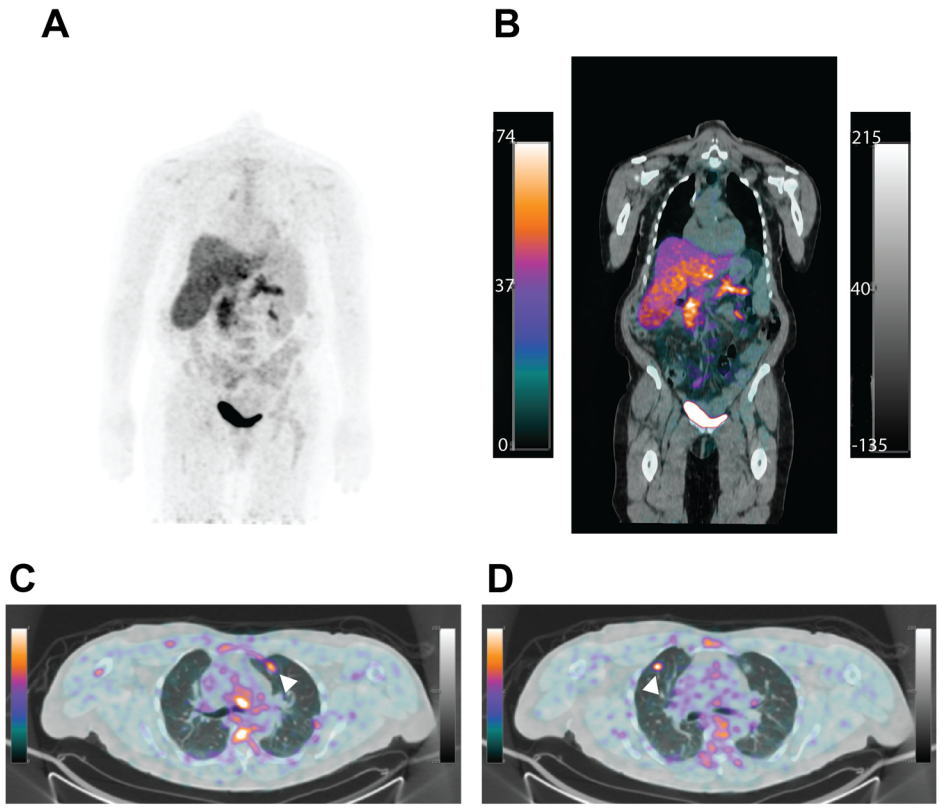

Figure 3: ^{11}C-glutamine biodistribution and tumor imaging in a patient with metastatic colorectal cancer. Whole-body PET (**A**) and PET/CT fusion (**B**) images of ^{11}C-glutamine showing normal organ accumulation. High uptake was seen in the bladder, liver, and pancreas. Axial ^{11}C-glutamine PET/CT fusion images corresponding to two lung nodules (**C** and **D**). White arrowheads point to the lesions. The lesion-to-blood pool ratios from the whole-body scan were 2.17 (**C**) and 2.59 (**D**).

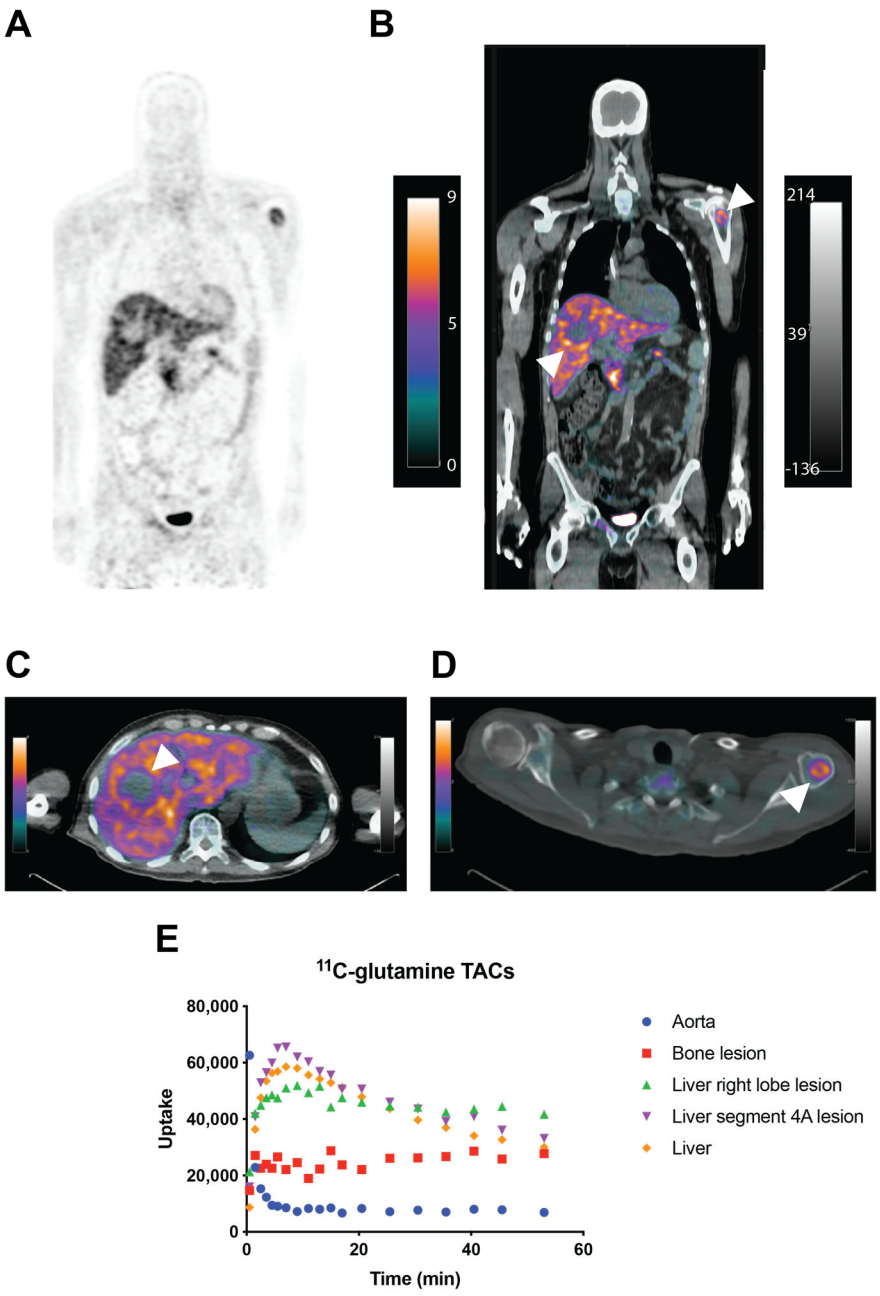

Figure 4: ^{11}C-glutamine biodistribution and tumor imaging in a patient with metastatic colorectal cancer. Whole-body PET (**A**) and PET/CT fusion (**B**) images of ^{11}C-glutamine showing normal organ accumulation and several metastases. High uptake was seen in the bladder, liver, and pancreas. Axial ^{11}C-glutamine PET/CT fusion images corresponding to a liver metastasis (**C**) and a left humeral head metastasis (**D**). White arrowheads point to the lesions. The lesion-to-blood pool ratios from the whole-body scan were 5.33 (**C**) and 4.02 (**D**). The lesion-to-liver ratio from the whole-body scan was 1.66 (**C**). Time-activity curves (**E**) for the aorta (blue circles), liver (orange diamonds), liver lesions (green and purple triangles), and bone metastasis (red squares).

Table 1: Cumulative activity (Bq-h/Bq) of ^{11}C-glutamine in organs of interest for each patient

N (Bq-h/Bq)	Patient 1	Patient 2	Patient 3
Adrenals	0.00026	0.00016	0.00010
Small Intestine	0.00679	0.00493	0.00389
Stomach	0.00256	0.00078	0.00155
Heart	0.00582	0.00424	0.00355
Right Kidney	0.00316	0.00427	0.00199
Left Kidney	0.00317	0.00372	0.00195
Liver	0.09487	0.06391	0.07328
Pancreas	0.00421	0.00374	0.00302
Bone Marrow	0.02184	0.02638	0.01318
Bladder	0.00905	0.01345	0.00856
TOTAL	0.15175	0.12557	0.11106
Remainder	0.33788	0.36405	0.37857

Table 2: Dosimetry estimates for adult subjects based on dynamic PET imaging with ^{11}C-glutamine.

(mGy/MBq)	Patient 1	Patient 2	Patient 3	Mean	SD	COV (%)
Adrenals	7.51E-03	5.53E-03	3.61E-03	5.55E-03	1.95E-03	35%
Brain	2.47E-03	2.66E-03	2.13E-03	2.42E-03	2.69E-04	11%
Breasts	2.59E-03	2.67E-03	2.15E-03	2.47E-03	2.80E-04	11%
Gallbladder Wall	5.44E-03	4.81E-03	4.17E-03	4.81E-03	6.35E-04	13%
LLI Wall	3.42E-03	3.69E-03	2.83E-03	3.31E-03	4.40E-04	13%
Small Intestine	5.60E-03	5.08E-03	2.99E-03	4.56E-03	1.38E-03	30%
Stomach Wall	5.01E-03	3.94E-03	2.93E-03	3.96E-03	1.04E-03	26%
ULI Wall	3.89E-03	3.87E-03	3.04E-03	3.60E-03	4.85E-04	13%
Heart Wall	5.57E-03	4.94E-03	3.90E-03	4.80E-03	8.43E-04	18%
Kidneys	8.27E-03	9.65E-03	5.14E-03	7.69E-03	2.31E-03	30%
Liver	2.21E-02	1.53E-02	1.31E-02	1.68E-02	4.69E-03	28%
Lungs	3.41E-03	3.37E-03	2.67E-03	3.15E-03	4.16E-04	13%
Muscle	2.93E-03	3.06E-03	2.47E-03	2.82E-03	3.10E-04	11%
Ovaries	3.53E-03	3.76E-03	2.93E-03	3.41E-03	4.29E-04	13%
Pancreas	1.53E-02	1.35E-02	1.01E-02	1.30E-02	2.64E-03	20%
Red Marrow	4.65E-03	5.16E-03	3.58E-03	4.46E-03	8.06E-04	18%
Osteogenic Cells	6.06E-03	6.67E-03	4.29E-03	5.67E-03	1.24E-03	22%
Skin	2.32E-03	2.45E-03	1.99E-03	2.25E-03	2.37E-04	11%
Spleen	3.45E-03	3.54E-03	2.76E-03	3.25E-03	4.27E-04	13%
Testes	NA	NA	2.36E-03	2.36E-03	NA	NA
Thymus	3.06E-03	3.16E-03	2.52E-03	2.91E-03	3.44E-04	12%
Thyroid	2.62E-03	2.81E-03	2.41E-03	2.61E-03	2.00E-04	8%
Urinary Bladder Wall	1.09E-02	1.51E-02	8.26E-03	1.14E-02	3.45E-03	30%
Uterus	3.63E-03	3.93E-03	3.06E-03	3.54E-03	4.42E-04	12%
Total Body	3.61E-03	3.58E-03	2.83E-03	3.34E-03	4.42E-04	13%
Effective Dose Equivalent (mSv/MBq)	6.34E-03	6.20E-03	4.46E-03	5.67E-03	1.05E-03	18%
Effective Dose (mSv/MBq)	4.96E-03	4.85E-03	3.58E-03	4.46E-03	7.67E-04	17%

LLI = lower large intestine
ULI = upper large intestine
SD = standard deviation
COV = coefficient of variation

Table 3: Quantification of ^{11}C-glutamine uptake in tumors.

Patient Number	Lesion Location	Lesion-to-Blood Pool Ratio*	Shown in Figure
1	Right posterior hepatic lobe	5.40	Supplemental Figure 3A
	Right adrenal	3.50	Supplemental Figure 3C
	Lung LUL	2.17	Figure 3C
	Liver segment 4A	5.11	Supplemental Figure 3B
	Lung RUL	2.59	Figure 3D
	Lung posterior LUL	1.93	Supplemental Figure 3D
3	Bone T12	3.24	Not shown
	Liver right lobe	5.33	Figure 4C
	Liver segment 4A	3.91	Not shown
	Bone left humeral head	4.02	Figure 4D
8	Lung RLL	1.65	Not shown
	Lung LLL	2.54	Not shown
	Lung LUL	2.64	Figure 2A
	Lung LUL	1.17	Not shown
	Lung RUL	2.22	Figure 2B (top)
	Lung RLL	2.56	Not shown
	Brain	1.68	Figure 2C
	Lung posterior RLL	2.35	Figure 2B (bottom)

*The ratios of the maximum value in the lesion to the average value in the blood pool from whole-body images are given for each lesion as described in the Materials and Methods.
LUL = left upper lobe
RUL = right upper lobe
RLL = right lower lobe
LLL = left lower lobe

Graphical Abstract

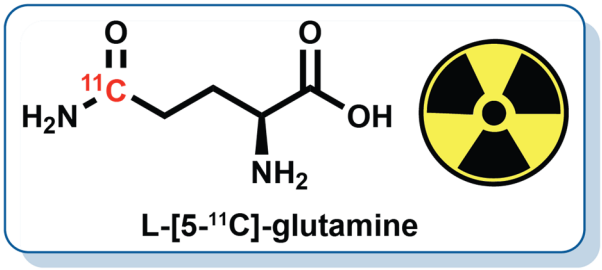

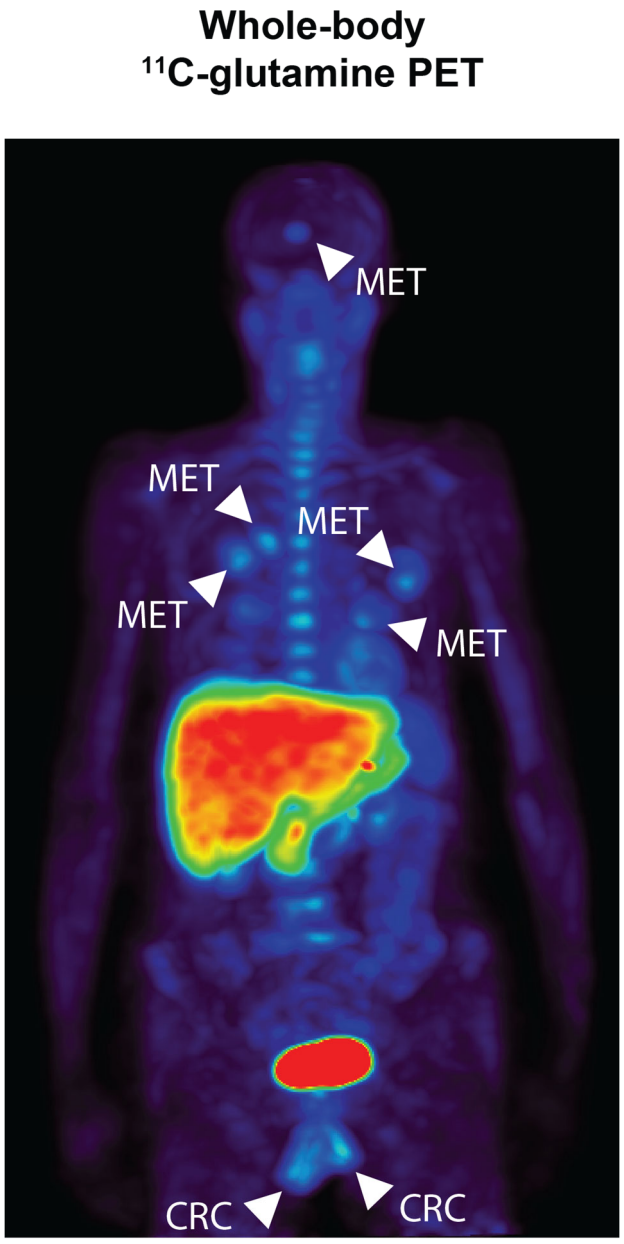

Supplemental Data

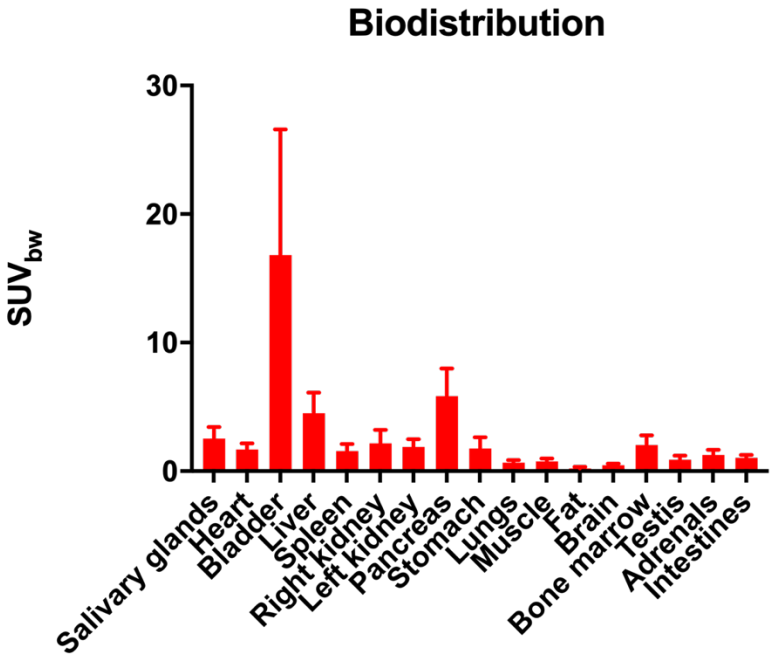

Supplemental Figure 1: Whole-body biodistribution of ^{11}C-glutamine uptake in normal tissues. The standard uptake value (SUV), normalizing by body weight (bw), is plotted for 1-hour post-injection.

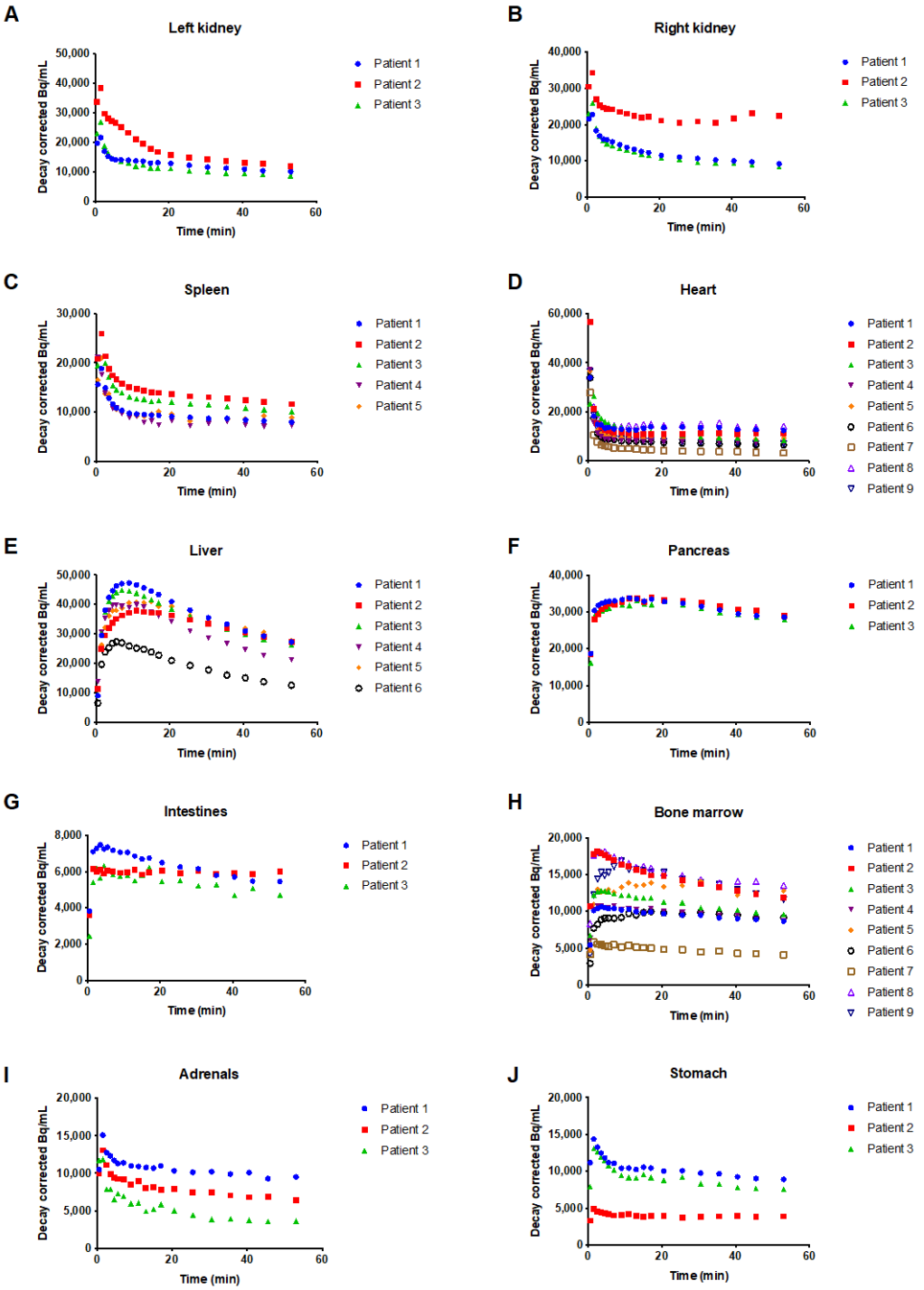

Supplemental Figure 2: Dynamic PET analysis of ^{11}C-glutamine uptake in normal tissues. The activity concentration (Bq/mL) decay-corrected to the time of injection is plotted over time for each organ. Shown are data for (**A**) Left kidney, (**B**) Right kidney, (**C**) Spleen, (**D**) Heart, (**E**) Liver, (**F**) Pancreas, (**G**) Intestines, (**H**) Bone marrow, (**I**) Adrenals, and (**J**) Stomach.

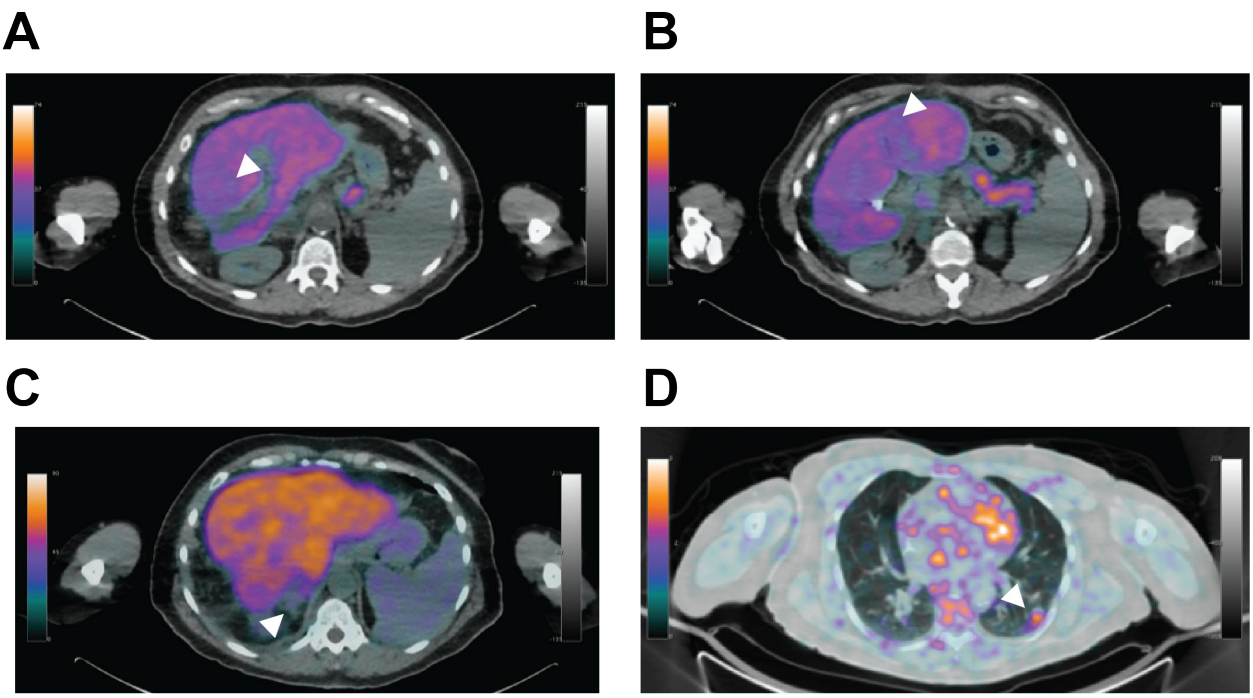

Supplemental Figure 3: ^{11}C-glutamine tumor imaging in a patient with metastatic colorectal cancer. Axial ^{11}C-glutamine PET/CT fusion images corresponding to two liver lesions (**A** and **B**), an adrenal mass (**C**), and a lung nodule (**D**). White arrowheads point to the lesions. The lesion-to-blood pool ratios from the whole-body scan were 5.40 (**A**), 5.11 (**B**), 3.50 (**C**), and 1.93 (**D**). The lesion-to-liver ratios from the whole-body scan were 1.19 and 1.13 for **A** and **B**, respectively.

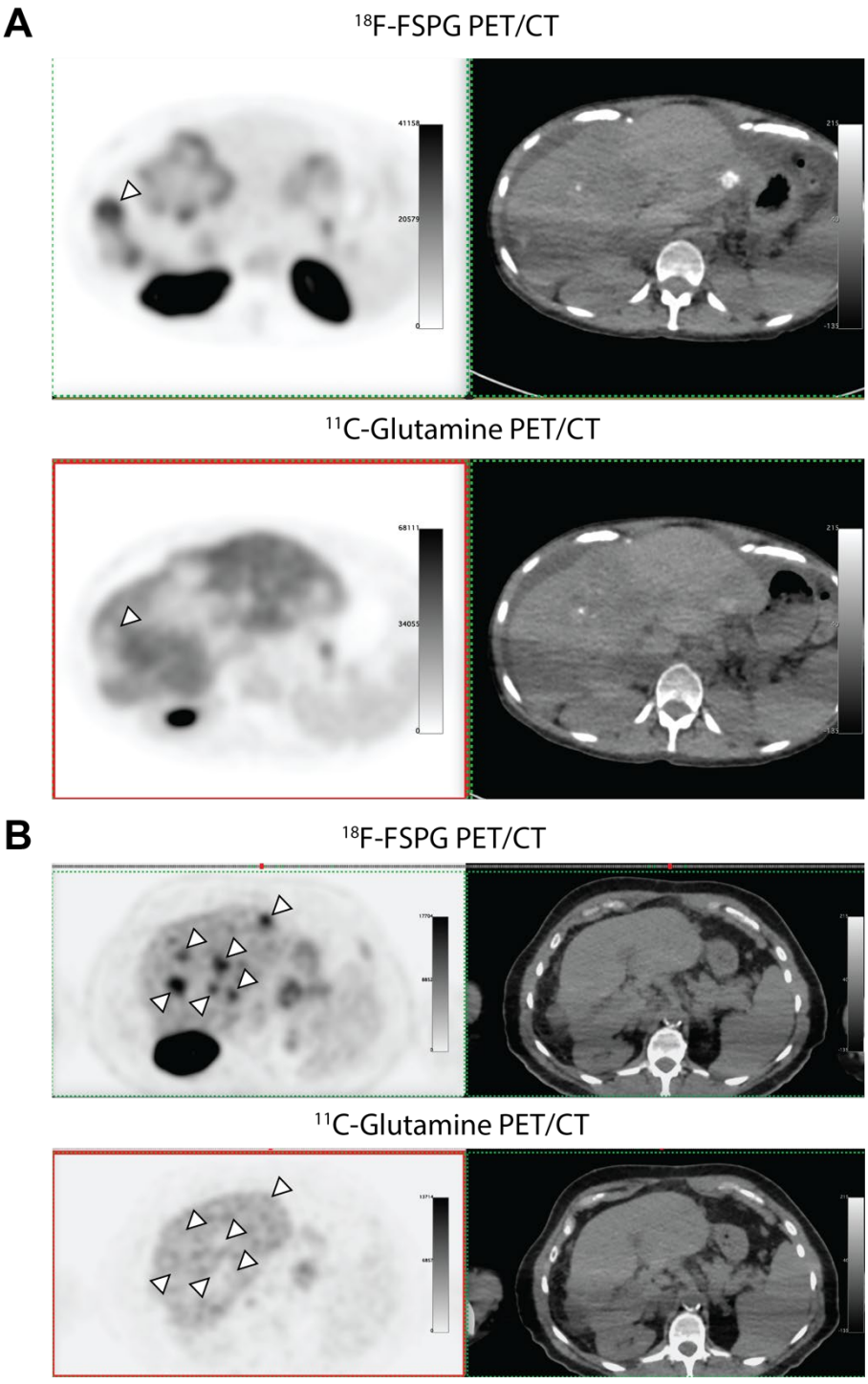

Supplemental Figure 4: ^{11}C-glutamine negative tumors in patients with metastatic colorectal cancer. ^{18}F-FSPG is an investigational PET radiotracer being evaluated for tumor imaging (*50,51*). Axial ^{18}F-FSPG PET images with corresponding CTs (upper images) show (**A**) a right lateral liver lesion and (**B**) multiple hepatic metastases. The corresponding locations on axial ^{11}C-glutamine PET images (lower images) demonstrate a lack of tumor uptake. White arrowheads point to the lesions.